Determining oxygen relaxations at an interface : a comparative study between transmission electron microscopy techniques

Determining oxygen relaxations at an interface: A comparative study between transmission electron microscopy techniques

N. Gauquelin[a,1], K.H.W. van den Bos[a,1], A. Béché[a], F.F. Krause[b], I. Lobato[a], S. Lazar[c], A. Rosenauer[b], S. Van Aert[a], J. Verbeeck[a,*]

[a] *Electron Microscopy for Materials Science (EMAT), University of Antwerp, Groenenborgerlaan 171, 2020 Antwerp, Belgium*
[b] *Institute for Solid State Physics, University of Bremen, Otto-Hahn-Allee 1, 28359 Bremen, Germany*
[c] *FEI Company, Achtseweg Noord 5, 5651 GG Eindhoven, The Netherlands*

Abstract

Nowadays, aberration corrected transmission electron microscopy (TEM) is a popular method to characterise nanomaterials at the atomic scale. Here, atomically resolved images of nanomaterials are acquired, where the contrast depends on the illumination, imaging and detector conditions of the microscope. Visualization of light elements is possible when using low angle annular dark field (LAADF) STEM, annular bright field (ABF) STEM, integrated differential phase contrast (iDPC) STEM, negative spherical aberration imaging (NCSI) and imaging STEM (ISTEM). In this work, images of a $NdGaO_3$-$La_{0.67}Sr_{0.33}MnO_3$ (NGO-LSMO) interface are quantitatively evaluated by using statistical parameter estimation theory. For imaging light elements, all techniques are providing reliable results, while the techniques based on interference contrast, NCSI and ISTEM, are less robust in terms of accuracy for extracting heavy column locations. In term of precision, sample drift and scan distortions mainly limits the STEM based techniques as compared to NCSI. Post processing techniques can, however, partially compensate for this. In order to provide an outlook to the future, simulated images of NGO, in which the unavoidable presence of Poisson noise is taken into account, are used to determine the ultimate precision. In this future counting noise limited scenario, NCSI and ISTEM imaging will provide more precise values as compared to the other techniques, which can be related to the mechanisms behind the image recording.

Keywords: High-resolution (scanning) transmission electron microscopy (HR (S)TEM), Quantitative electron microscopy, Statistical parameter estimation theory, Interfaces in perovskite materials

1. Introduction

In order to go beyond silicon technology limitations, many researches are now focussing on the development of new electronic devices based on oxide materials [1]. Here, perovskite materials are among the most promising materials. With a typical atomic formula ABO_3, A and B representing two different cations, perovskites are characterized by an octahedron of oxygen atoms located around the central B atom, forming the BO_6 formula-unit. These oxygen atoms produce a crystal field around the B atom, thereafter influencing the many degrees of freedom of this same B atom (spin, orbital, charge, etc...) and giving rise to new physical properties. At the interface between two of these perovskite materials, new exotic electronic properties can arise which are not present in the separate bulk material [2, 3], such as two dimensional electron gas (i.e. $LaAlO_3/SrTiO_3$) [4], interfacial superconductivity (i.e. $La_{1-x}Ca_xMnO_3/YBa_2Cu_3O_7$) [5, 6, 7] or ferroelectric tunnel junctions [8]. The ionic radius of the A and B cations can introduce a tilt of the octahedron as a result of an optimization of the lattice through distortions from the ideal Pm3m cubic structure towards the energetic minimum configuration [9]. Neighbouring octahedra can in addition tilt in-phase and out-of-phase of each other in different directions giving rise to many different variations and space groups [10, 11, 12]. As this modifies the volume of the unit cell, it can accommodate stress and even change the above mentioned degrees of freedom and electronic structure of the B atom in its BO_6 environment drastically. Another interfacial effect that can give rise to new properties is oxygen octahedral coupling, where the octahedral tilt is transferred from one perovskite material into the other [13, 14, 15, 16, 17]. In order to understand the physical properties of oxide materials, it is mandatory to characterise these interfaces down to the atomic scale. As these interfaces are buried inside the material, they are not easily accessible to the commonly used X-Ray or neutron techniques except in very specific and dedicated experiments such as Resonant X-Ray reflectivity [18]. Thanks to the general availability of aberration correctors for the last decade [19, 20, 21], transmission electron microscopy (TEM) is now capable of characterising materials with a sub-ångström resolution [22, 23, 24]. Thereafter, TEM has become the most common way to look at oxide interfaces and to visualize the oxygen octahedral rotations.

Nowadays, five main techniques are accessible to TEM microscopists for imaging light atoms such as oxygen: low angle annular dark field (LAADF) scanning transmission electron microscopy (STEM), annular bright field (ABF) STEM, integrated differential phase contrast (iDPC) STEM, negative Cs imaging

*Corresponding author
Email address: jo.verbeeck@uantwerpen.be (J. Verbeeck)
[1] Both authors contributed equally to this work.

(NCSI), and imaging STEM (ISTEM). Schematics of the different techniques are shown in Fig. 1(a). In STEM, scattered electrons formed by a sub-ångström convergent probe which is raster scanned over the surface of the sample are collected on an extended disk or annular detector. For LAADF-STEM, the inner angle of the detector is slightly higher as compared to the probe semi-convergence angle while the outer angle is limited by the detector geometry. This setup gives rise to images of bright atomic columns on a dark background [25] , where the atomic contrast mainly depends on the atomic number of the element. In ABF STEM, the angular range of the detector lies within the bright field disk defined by the semi-convergence angle of the probe. The recorded image consists of atomic columns with black contrast on a white background [26, 27]. Recently, iDPC STEM [28] has been introduced as a new promising TEM technique to map both light and heavy elements at the atomic scale. Similar as in the differential phase contrast (DPC) technique introduced by Rose [29], iDPC STEM imaging relies on the difference in intensities between two or more quadrants of an annular STEM detector [30]. In iDPC STEM, the recorded difference maps are used to perform an integration in Fourier space, resulting in an image where the contrast is related to the projected electrical potential in the sample [28]. In NCSI, the specimen is illuminated by an electron plane wave followed by an image corrector which aberrations are tuned to provide a negative spherical aberration (Cs) component to the electron wave function. The obtained image of a crystal gains a high contrast where all atomic columns appear as bright dots on a dark background [31, 32]. Another recently developed technique is ISTEM [33], where STEM illumination is combined with conventional TEM imaging. The resulting image is more robust to probe instabilities and scan noise errors as compared to the other STEM based techniques. The contrast in the image is, although dependent on defocus, highly sensitive to both light and heavy atomic columns.

All these TEM based techniques are capable of visualising light atomic columns with sub-Ångström resolution, enabling qualitative evaluations. However, the characterization of materials requires a quantitative extraction of structural information with picometer precision, as displacements of atoms in this range can already alter the materials properties [34, 35]. Note that precision corresponds to the standard deviation with which these structure parameters can be measured from noisy images. Statistical parameter estimation theory has proven to be an efficient technique for quantitatively retrieving atomic column positions from high resolution TEM images [36, 37, 38, 39]. Based on this method, a substrate-film interface in a model system $La_{0.67}Sr_{0.33}MnO_3$-$NdGaO_3$ has been investigated to quantitatively compare NCIS, ABF STEM, LAADF STEM, IDPC STEM and ISTEM for mapping atomic columns. High angle annular dark field (HAADF) STEM imaging is used as a standard to compare the extracted positions of the heavy atoms.

2. Experiment and simulations

A TEM lamella of an $NdGaO_3$ (NGO) substrate with a thin layer of 20 unit cells of $La_{0.67}Sr_{0.33}MnO_3$ (LSMO), epitaxially grown on top of it by Pulsed laser deposition (PLD) [17], was prepared in cross section by focused ion beam (FIB) milling to a thickness of approximately 16 nm according to image simulations (see Section 2.5). In the final sample, the electron beam propagates along the $[001]_o$ direction with the $[1\bar{1}0]_o$ direction along the interface and the $[110]_o$ direction along the growth direction, perpendicular to the interface. In this work, the relaxation of octahedral tilt of the BO_6 octahedron when going from the $NdGaO_3$ substrate to the $La_{0.67}Sr_{0.33}MnO_3$ film gives a unique opportunity to quantitatively compare the different TEM techniques that allow the visualization of light elements. All TEM images have been acquired on probe and image Cs corrected FEI instruments operated at 300kV. iDPC images have been recorded on a Titan^3 Thalos microscope at the FEI Nanoport (Eindhoven, The Netherlands), while images from all other techniques have been recorded at the QuAntEm, a Titan^3 microscope (University of Antwerp, Belgium). More information on the specific set-ups and microscope parameters used for each technique is given in the following.

2.1. ADF and ABF STEM

When using STEM based techniques, a focussed electron probe is scanned over the surface of the sample. Per probe position the integrated scattered signal in the diffraction space is recorded for a certain angular range, which defines the contrast of the final image.

The HAADF, LAADF and ABF STEM images of the LSMO-NGO sample are displayed in Fig. 1(b-d). All images are recorded with a probe semi-convergence angle of 19.8 mrad and a beam current of 40 pA. The HAADF and LAADF images are recorded on a Fischione Model 3000 detector, while the ABF images are recorded on a Gatan dark field (DF) detector. The used camera lengths with their corresponding collection angles for the different detectors are given in Table 1. Despite the incoherent image formation in LAADF STEM, there is a narrow angular range where light elements, such as oxygen, may be detectable [25, 40]. In fact, image simulations suggest that the LAADF region is most optimal for mapping light atomic columns in very thin crystals of only a few nanometres thick, while only for thicker crystals the ABF regime is best [40, 41]. In Fig. 1(c), some weak contrast of the oxygen atomic columns can be seen in between the relatively heavy La/Sr, Mn, Nd and Ga atomic columns. It is important to remark that for these STEM techniques, the contrast depends on the atomic number of the elements and very weakly depends on the probe focus. The larger the collection angle is, the more robust the technique is towards astigmatism and higher order aberrations.

Technique	Detector	Collection Angles	CL
HAADF	Fischione 3000	44-190 mrad	115 cm
LAADF	Fischione 3000	22-136 mrad	230 cm
ABF	Gatan DF	8-17 mrad	115 cm

Table 1: Experimental collection angles and camera lengths (CL) used for the different imaging techniques.

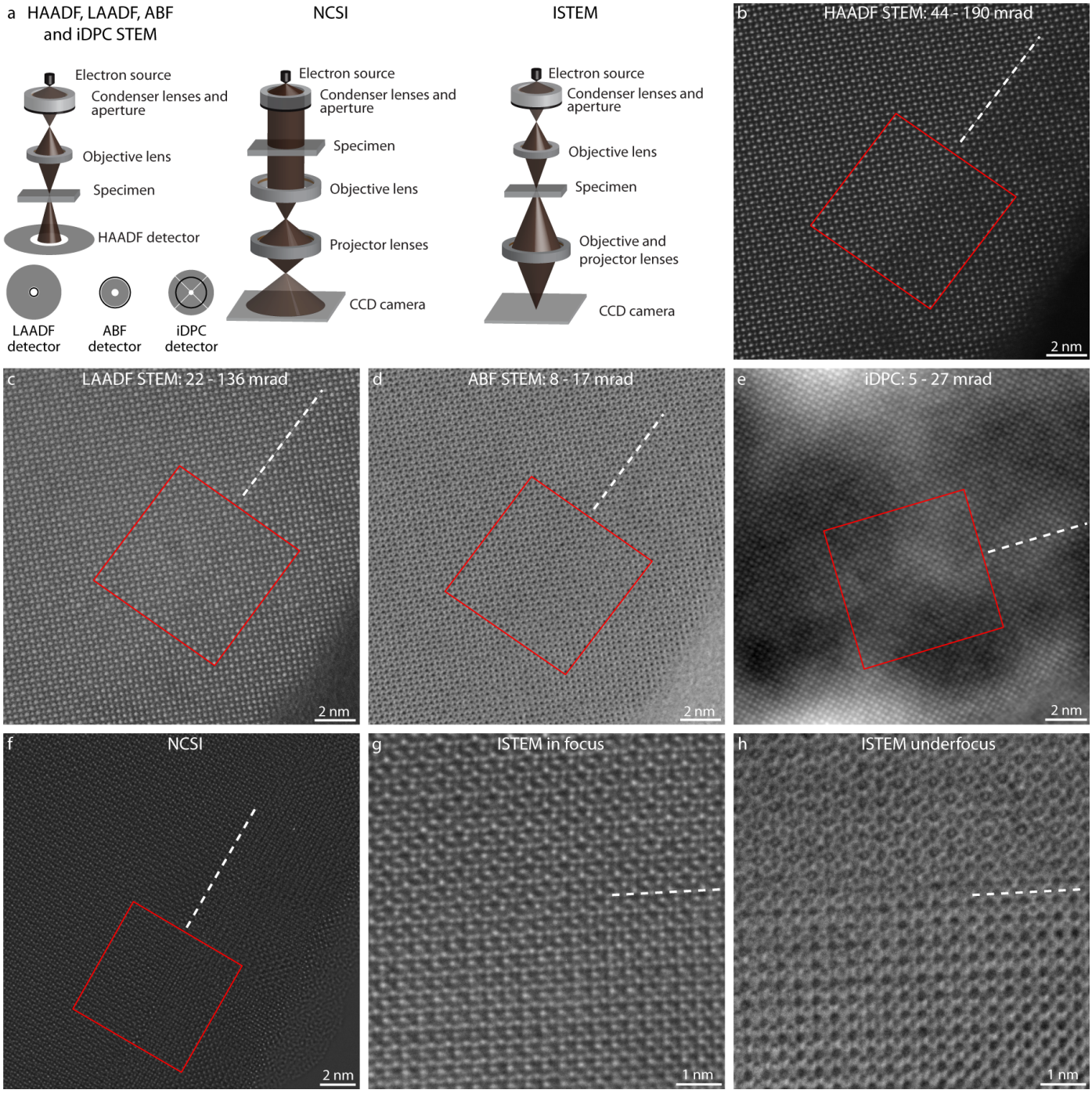

Figure 1: (a) Schematics of the different used TEM techniques. For the STEM based techniques the different detector geometries are shown, where the black circle indicates the probe semi-convergence angle. Experimental images of an LSMO-NGO interface recorded by (b) HAADF STEM, (c) LAADF STEM, (d) ABF STEM (e) iDPC, (f) NCSI, (g) ISTEM in focus and (h) under focussed ISTEM imaging. The white dotted line marks the interface. An area of 18 x 18 unit cells around the interface, marked in red, indicates the region used for the statistical analysis. In the ISTEM images the full field of view has been used for analysis.

2.2. iDPC

Recently, Lazic et al. [28] introduced the new iDPC STEM technique, which is sensitive to both light and heavy elements. This STEM technique is based on differential phase contrast [29, 42, 43], where for each scanning position an approximation of the centre of mass (COM) is obtained by measuring the difference in intensity between two or more quadrants of an annular STEM detector. Next, the resulting COM image is integrated in the Fourier domain, resulting in an image that is related to the phase shift caused by the sample. For non-magnetic samples, this phase shift can be related to the electrostatic potential of the sample. Lazic et al. [28] have shown that for this purpose, a four quadrant annular detector can be used. In this work, an image (Fig. 1(e)) is recorded with a probe semi-convergence angle of 19.8 mrad and a beam current of 10 pA. The contrast is found to be dependent on the correct adjustment of the gain of the four quadrants and on the probe aberrations. It can be observed that the image contrast in Fig. 1(e) slowly varies, which may be explained by the high sensitivity of the formed image to any phase modifications, especially surface imperfections induced by FIB milling. The FEI DF4 detector is used at a camera length of 285 cm, corresponding to a collection angle of 5-27 mrad. Image simulations have been used to identify the different atomic column types.

2.3. NCSI

Negative Cs imaging (NCSI) is very similar to the well-established high resolution TEM technique, except that the spherical aberration is purposely turned slightly negative to allow the visualization of light atomic colums. In Fig. 1(f), a NCSI image is shown, recorded on a 2k × 2k Gatan US1000 camera at a magnification of 800 kX. The spherical aberration of the image corrector has been tuned to -12.9 μm ± 2.5 μm, which is commonly used for this imaging technique [31, 32, 44, 45, 46]. As the contrast in this technique is strongly dependent on aberrations (1st and 2nd order aberrations *i.e.* focus, astigmatism and coma) and the sample thickness [31, 44], interpretation is not as straightforward as for the conventional STEM-based techniques. Therefore, image simulations have been used in order to identify each specific type of atomic column [31, 32].

2.4. ISTEM

For this technique, images which are sensitive to both light and heavy elements are recorded by combining STEM illumination with TEM imaging [33]. The electron probe, in image mode, is raster scanned over the sample while the resulting signal is recorded in a single frame on a CCD camera. Here, the signal was recorded on a Gatan US1000XP camera located behind a Gatan Image Filter (GIF) operating in standard imaging mode. With the choice of both objective and condenser aperture, ISTEM offers two free parameters for the experimental setup. In the presented experiment, a probe semi-convergence angle of 8 mrad together with a TEM magnification of 295 kX and a beam current of 40 pA have been used to acquire both an in focus and an underfocused image (see Figs. 1(g) and 1(h)). No objective aperture was applied. This setup is similar to the original configuration used in [33] and constitutes a compromise between resolution and contrast. By further variation of the apertures, the ISTEM contrast can be tuned. However, such a study is beyond the scope of this paper. The spherical aberration of both the probe and the image corrector have been minimized bellow 1 μm. As the image contrast is atom type and thickness dependent, image simulations are required to identify the different column types. It is further important to point out that imaging aberrations have a strong influence on the image and can even lead to contrast reversal, while probe aberrations have no influence whatsoever.

2.5. Image simulations

In order to assess that the optimal experimental imaging conditions are fulfilled for visualizing the oxygen atomic columns of the LSMO/NGO sample with the highest possible contrast, image simulations have been performed for each experimental technique (Fig. 2). Here, the STEMsim program [47] has been used under the multislice approach with absorptive potentials to simulate images of the NGO-LSMO interface (Fig. 2(h)). Up to a thickness of about 20 nm, this approach has been shown to agree with frozen lattice calculations for STEM imaging [48]. Simulations have been performed for a range of thicknesses in order to estimate the exact experimental thickness to approximately 16 nm. The microscope focus and astigmatism are then finely tuned to best match the simulated images. The parameters of the different simulations are summarized in Appendix A. The simulated images of the LSMO-NGO interface are presented in Fig 2 together with insets of the experimental images to highlight the qualitative match between the experimental images and the simulations. The simulated HAADF, LAADF and ABF STEM images show an excellent agreement with the experimental images, while small discrepancies are present in the other techniques. These small discrepancies may be explained by the high sensitivity of the image contrast in iDPC STEM, NCSI and ISTEM imaging to aberrations and surface imperfections, the latter being neglected in the image simulations.

3. Methodology

In order to compare all experimental techniques in a reliable and quantitative manner, the atomic column positions have been extracted by using the StatSTEM software [39]. Here, statistical parameter estimation theory is used to model the atomic columns as Gaussian peaks:

$$f_{k,l}(\boldsymbol{\theta}) = \zeta + \sum_{i=1}^{I} \sum_{m_i=1}^{M_i} \eta_{m_i} \exp\left(-\frac{\left(x_k - \beta_{x_{m_i}}\right)^2 + \left(y_l - \beta_{y_{m_i}}\right)^2}{2\rho_i^2} \right) \quad (1)$$

where ζ is a constant background, ρ_i the width of a Gaussian peak of a particular column type i, η_{m_i} the height of the m_i^{th} Gaussian peak, $\beta_{x_{m_i}}$ and $\beta_{y_{m_i}}$ the x- and y-coordinate of the m_i^{th} atomic column, respectively. In the model, the unknown structure parameters are given by the parameter vector: $\boldsymbol{\theta} = (\beta_{x_{1_1}} \cdots \beta_{x_{M_I}}, \beta_{y_{1_1}} \cdots \beta_{y_{M_I}}, \rho_1 \cdots \rho_I, \eta_{1_1} \cdots \eta_{M_I}, \zeta)^T$.

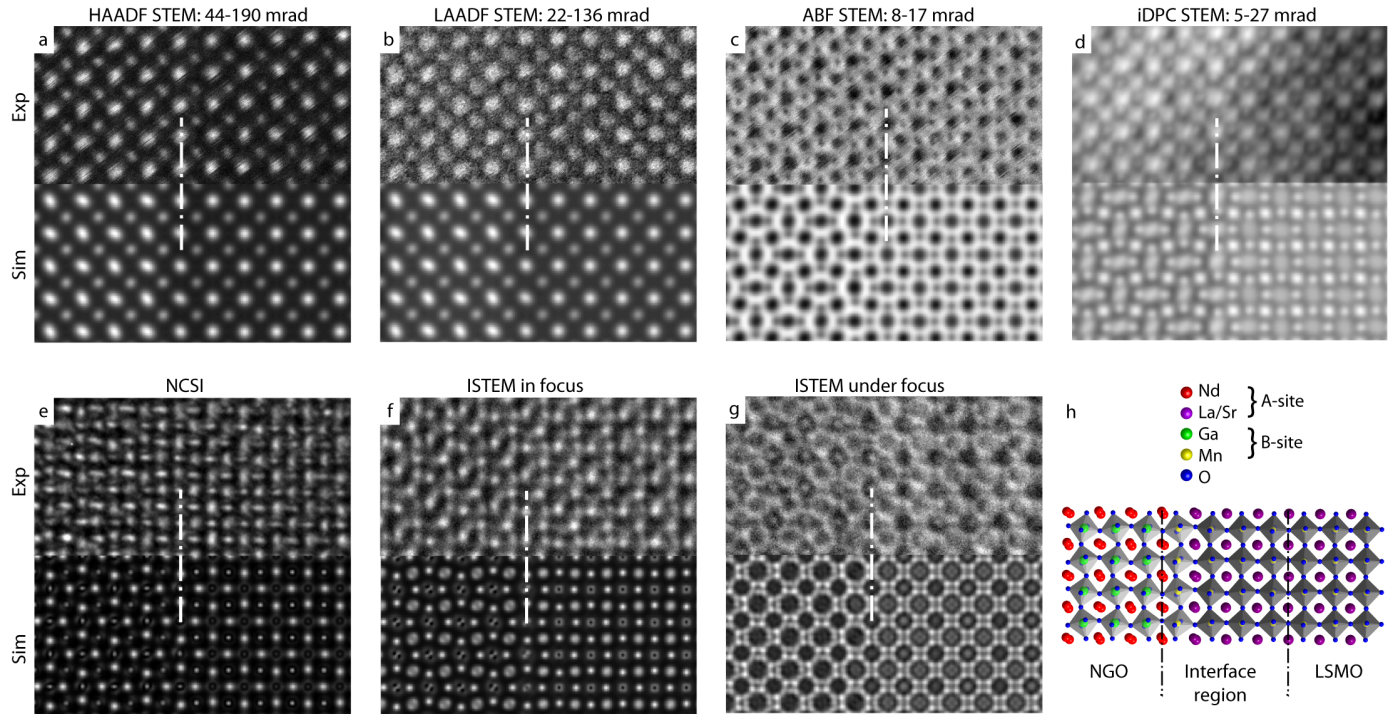

Figure 2: Experimental (top half of the panel) and simulated (bottom half of the panel) images for the different techniques investigated: (a) HAADF STEM, (b) LAADF STEM, (c) ABF STEM, (d) iDPC STEM, (e) NCSI, (f) ISTEM in focus and (g) underfocus (f). The white dashed line is a guide to the eye of the location of the interface (h) Atomistic model of the NGO-LSMO interface used for the simulations.

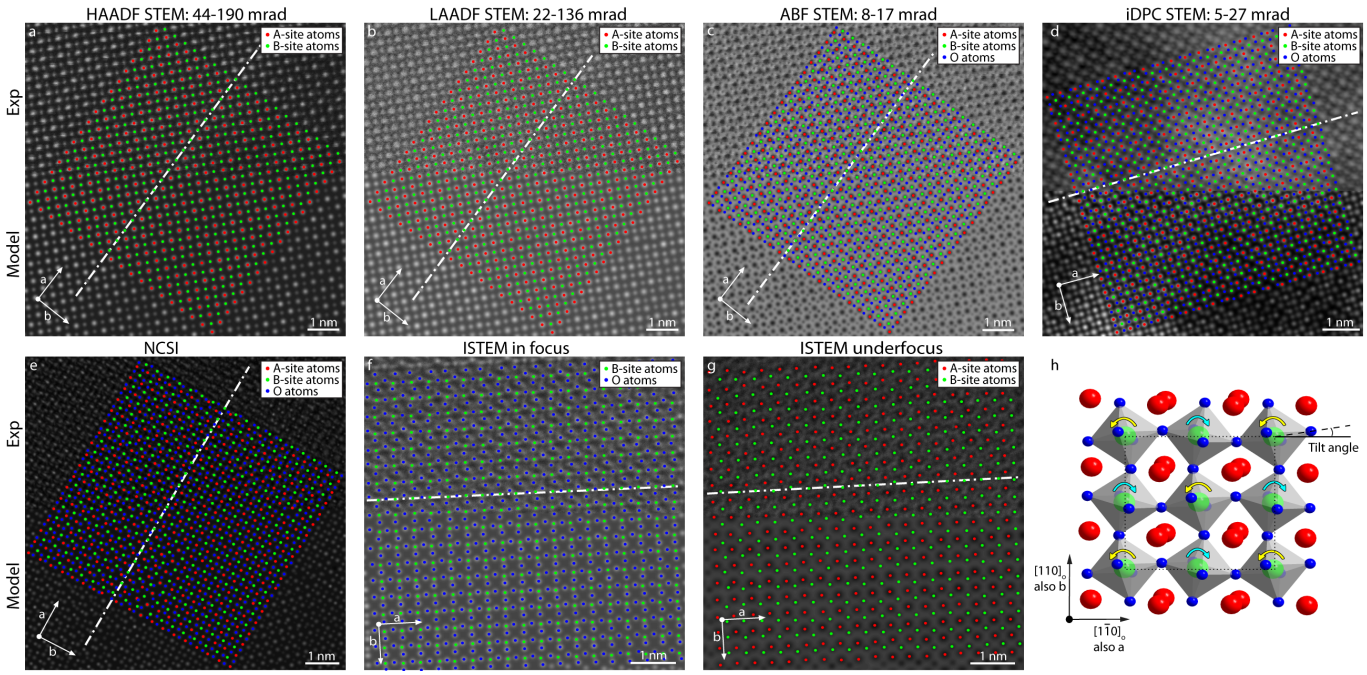

Figure 3: (a-g) The experimental images (top part) with the fitted Gaussian models (bottom part) of the selected regions around the interface (marked by a white dotted line). The estimated column positions are shown as an overlay. (h) Schematic of the octahedral tilt system of the oxygen columns in the NGO bulk material and its direction (clockwise in blue and anticlockwise in yellow).

In previous work, it is shown that this method is capable of extracting both accurately and precisely the atomic column positions from (S)TEM images [39, 49, 50]. Furthermore, it has been shown that for extracting atomic column positions also ISTEM images may be modelled as Gaussian peaks [51], since the contrast peaks at these positions. Therefore, these results indicate that despite the presence of a complex image formation process, Gaussian modelling is still valid for this purpose. In order to compare the different imaging techniques previously introduced, a region of 18 ×18 unit cells has been selected from all experimental images around the interface of LSMO and NGO (indicated by a red dotted-line square in Fig. 1). For the ISTEM images, the full field of view is used. As it is impossible to record all images simultaneously, small differences between the selected regions of interest for each technique might occur. In Fig. 3, the experimental images (top part) and the fitted Gaussian models (bottom part) of the selected regions for each imaging technique are shown together with the estimated column positions.

4. Results and discussion

As explained in Section 3, statistical parameter estimation theory is used to extract the positions of the atomic columns. From these estimated column positions, visualised in Fig. 3, each technique is independently characterised in terms of accuracy and precision. Depending on the imaging technique, part or all of the different atomic column types are visible. From the ABF STEM, iDPC and NCSI images, the column positions of all different column types can be determined from a single image. As expected for HAADF STEM, the contrast of the oxygen columns is too low for extracting their positions. Also the LAADF STEM images could not provide any reliable information on the oxygen column positions. With a careful look at it, one can see some very weak contrast on the oxygen positions. The signal-to-noise ratio is, however, too low to make them quantifiable. This lack of contrast can be explained by the thickness of the TEM sample, for which LAADF STEM imaging is no longer the optimum [40, 41]. For ISTEM, it was not possible to acquire an image where all atomic column types could provide interpretable contrast in a single frame, in contrast to the image simulations where all different columns types are visible (Figs.2(f) and 2g). Consequently, the A and B sites atomic column positions have been extracted from an under focussed image while the B and O sites positions have been measured from in focus conditions.

4.1. Accuracy

In order to determine and compare the accuracy of each imaging technique, both the evolutions of the lattice parameter and the tilt angle of the oxygen BO_6 octahedron (B=Ga or Mn) across the LSMO-NGO interface are investigated. These parameters are studied as a function of distance from the interface, shown in Fig. 4. In the analysis, the a-direction is used to refer to the $[1\bar{1}0]_o$ direction along the interface and the b-direction to refer to the $[110]_o$ direction perpendicular to the interface (see Fig 3(h)). The HAADF STEM image served as a reference for the evolution of lattice parameter since this is an incoherent imaging technique for which it has been shown that it can accurately locate atomic column positions [52, 53, 54]. Furthermore, the image contrast in this imaging technique is more robust with respect to sample misalignments as compared to NCSI and ISTEM imaging [51]. The evolution of the octahedral tilt across the interface is compared to Ref. [17].

4.1.1. Lattice parameter

In order to determine the evolution of the lattice parameter across the interface, the lattice parameter and the error are estimated from the mean distance between neighbouring columns of the A-site atomic columns in both the a- and b-direction. Fig. 4 shows that the lattice parameter in the a-direction, parallel to the interface, remains constant at 3.863 Å, confirming the perfect epitaxial conditions between the LSMO film and the NGO substrate. On the contrary, an expansion of the lattice parameter in the b-direction is seen when going from the NGO bulk material to the LSMO substrate. By taking the HAADF STEM profiles as a reference, the profiles for LAADF, ABF and iDPC STEM match with the expected trends. For NCSI and ISTEM no clear lattice expansion can be observed due to large inaccuracies in the measured A-type column positions. These deviations can be explained by the atomic column contrast, which is highly sensitive to sample imperfections and microscope parameters such as focus and astigmatism. Furthermore, the low contrast of the oxygen column in the under focussed ISTEM image, used for this analysis, could harm the measured A-type column positions even more. It should, however, be noted that away from the interface the measured lattice parameters for both imaging techniques seem to become more constant, indicating that these values are more accurate. This could be explained by sample imperfections, which are most likely more present close to the interface than away from it. From these results, it seems that LAADF, ABF and iDPC STEM images give the best accuracy for determining the heavy A-type atomic column positions.

4.1.2. Octahedral tilt

As explained in the introduction, NGO bulk material is characterised by a strong octahedral tilt, where the oxygen columns are rotated around the B-site atom alternatively in a clockwise

Technique	Octahedral coupling	Bulk octahedral tilt	Bulk B-site tilt
ABF	5.6 ± 1.0 UC	7.8° ± 0.3°	0.1° ± 0.2°
iDPC	5.2 ± 1.1 UC	11.3° ± 0.3°	0.0° ± 0.2°
NCSI	2.9 ± 1.4 UC	9.1° ± 0.5°	0.1° ± 0.2°
ISTEM	4.4 ± 0.8 UC	10.7° ± 0.2°	0.1° ± 0.2°
Literature	± 4 UC [17]	9° − 10° [55]	0°

Table 2: Comparison of structural parameters of the LSMO-NGO interface extracted from the different imaging techniques with literature values. The second column shows the region around the interface that is affected by octahedral coupling. The third column highlights the octahedral tilt of the oxygen atoms in the NGO bulk material. The fourth column demonstrates that distortions do not harm the accuracy as no tilt is present in the B-site columns.

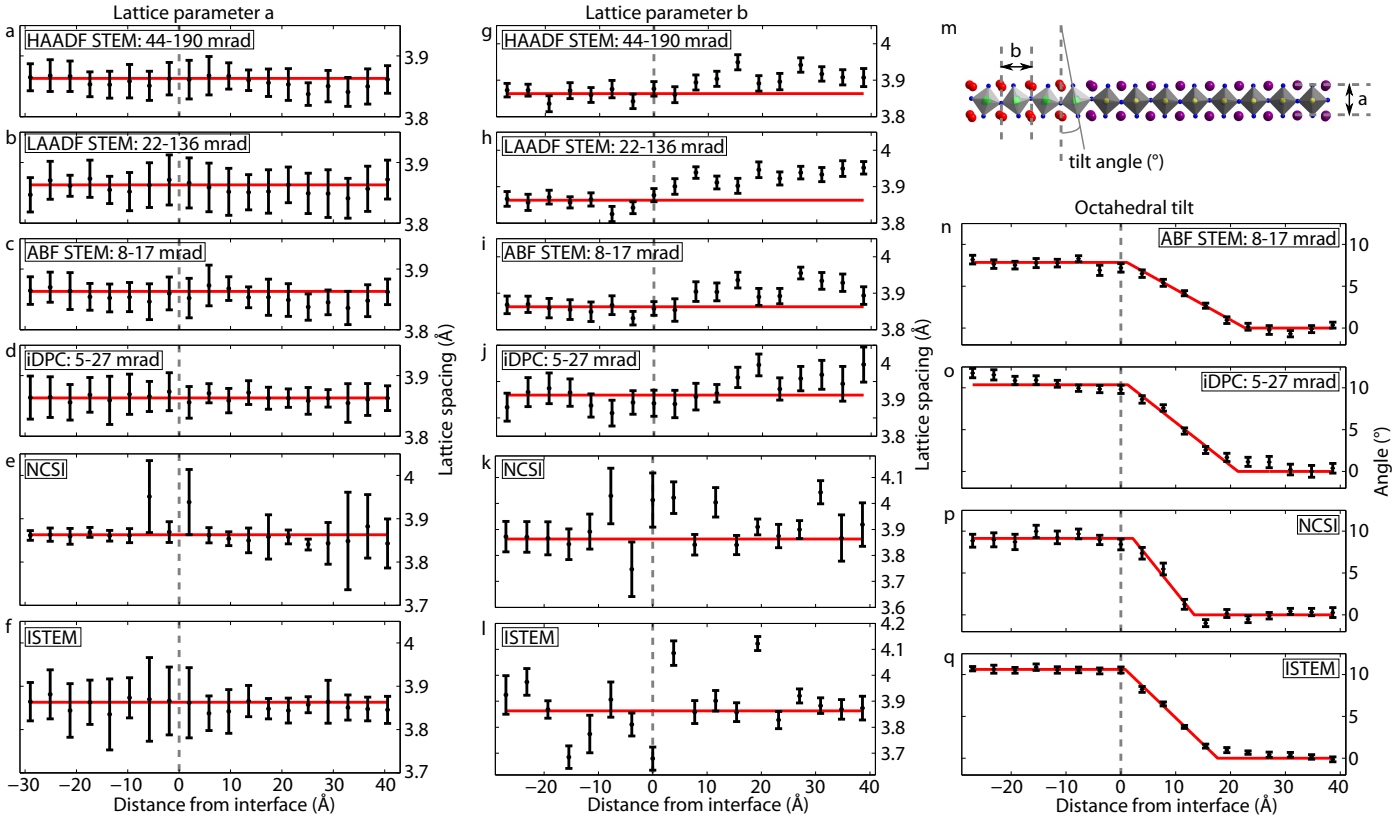

Figure 4: The mean lattice parameter (a-g) a and (g-l) b as a function of distance from the interface for the different imaging techniques. The bulk reference lattice parameter of 3.863 Å is shown in red in order to easily identify deviations. (m-p) The mean octahedral tilt of the oxygen BO6 octahedron as a function of distance from the interface for the different imaging techniques. The red curve represents a ramp function that is fitted in order to characterise the octahedral tilt around the interface. The grey dashed lines mark the expected interface position.

and anti-clockwise direction with respect to the direction of the lattice parameter in the a-direction (see Fig. 3(h)). In order to compare the capability of each technique to accurately visualise the light oxygen columns, the mean octahedral tilt is studied as a function of distance from the interface (see Fig. 4(m-p)). In this procedure, the a-direction is determined by fitting the B-site column positions layer by layer to a straight line parallel to the interface. Next, the 2 oxygen columns neighbouring the B-site column parallel to the a-direction are used to determine the angle of rotation with respect to the a-direction. Similar, a second measure of the octahedral tilt is obtained by using the 2 oxygen columns neighbouring the B-site atoms in the b-direction. Finally, the measurements from both directions are combined. In order to visualize the evolution of the octahedral tilt across the interface, the mean tilt angles as a function of distance from the interface are modelled by a ramp function as abrupt changes around the interface are expected. The size of the region around the interface that is affected by octahedral coupling is determined from the slope of this ramp function (see Table 2). For assessing the accuracy of the results, both the size of this affected region and the mean octahedral tilt in the NGO bulk region is investigated.

First, the mean octahedral tilt of the oxygen octahedron in the NGO region is investigated by using the 4 atomic planes that are furthest away from the interface in the studied region (see Table 2). Only small differences are found with respect to the reference value of the octahedral tilt in NGO bulk material, in between 9° and 10° [55]. It should be noted that the reference value is an experimental result obtained by neutron diffraction and inaccuracies may be present. This could therefore explain the small discrepancies between the measured values and the literature value. However, it does not explain the differences between the measured values obtained from the studied techniques. In order to verify whether the presence of image distortions are the cause of these differences, the angle between previously described mean a-direction and the local B-B directions per unit cell are evaluated. Again the 4 atomic planes that are furthest away from the interface have been used. The 4th column in Table 2 shows the mean angle with the corresponding error, indicating that image distortions are hardly affecting the measured octahedral tilt values. A close look at the profiles in Figs. 4(m-p) of the octahedral tilt along the interface reveals that the measured octahedral tilt in the NGO bulk region is constant, making it most likely that within each technique all measured oxygen column positions are shifted by approximately the same amount. Recently, it has been found that small misalignments of the sample in the microscope can shift the peak intensity away from the centre of an atomic column [51, 56**?**]. This shift in the peak intensity is constant for columns of the same type, which matches with the octahedral tilt observations

in the NGO bulk region. Therefore, it is expected that the small differences between the techniques are caused by small misalignments of the sample in the microscope. Note that images are not recorded simultaneously and misalignments differ per recorded image. As a result of this finding, small offsets still allow to investigate the evolution of the octahedral tilt along the interface on a relative basis.

The second column of Table 2 shows the size of the region affected by octahedral coupling, as is determined from the fitted ramp function to the octahedral tilt along the interface. The error is given by the 95% confidence bounds of the fitted parameters. Recently, Liao et al. [17] found by ABF STEM imaging and DFT calculations that strong octahedral coupling transfers the octahedral tilt, present in the NGO substrate, to approximately the first 4 planes of the LSMO film. The results of all imaging techniques match with this previous observation. The small differences between all values can be attributed either local interface roughness or to the presence of distortions, which are different per technique. In case of the STEM related techniques, one can correct for scan distortions and sample drift to further improve the results, as will be discussed in Section 4.3. The results on the octahedral tilt in the NGO bulk region show, however, that image distortions do most likely not affect the results. Nevertheless, scan distortions are less present in ISTEM and not present in NCSI in contrast to ABF and iDPC STEM. It may therefore still occur that the values in ABF STEM and iDPC STEM are a bit altered by scan distortion or sample drift. In iDPC STEM some further artefacts seem also to be present, as the octahedral tilt around the interface changes less abruptly. This could also affect the measured region that is affected by octahedral coupling. As compared to the other techniques, in NCSI the measured region affected by octahedral coupling is slightly lower. Furthermore, a close look at the results in Figs. 4(m-p) shows that the errorbars in NCSI are slightly higher as compared to the other techniques. These differences can be explained by the high sensitivity to aberrations of the objective lens, as is further discussed in Appendix B. Despite these differences, all measured values are overlapping with the reference value of about 4 unit cells which are affected by octahedral coupling, indicating that all techniques are capable of determining the octahedral tilt of the oxygen BO_6 octahedron across the interface accurately.

4.2. Precision

From Section 4.1 it has been found that all different techniques are capable to accurately measure the positions of the different column types. Only close to the interface, the heavy A-site column locations are measured with degraded accuracy from the NCSI and ISTEM images due to a contrast decrease. For the other STEM related techniques, the oxygen column positions are most likely measured with a small, constant offset in the NGO bulk region which may be explained by small sample misalignments. Therefore, the NGO bulk region can be used to investigate the precision with which atomic column positions can be measured.

The results from Section 4.1 suggest that the 4 atomic planes that are furthest away from the interface in the studied region are most likely not affected by the interface and can be used for precision measurements. In this bulk like region, the lattice parameter is determined by measuring the distance between neighbouring columns of the same type in the a-direction (parallel to the interface), as this direction was shown to be unstrained in the previous section. For the oxygen columns, every second unit cell is used to determine the lattice parameter as the oxygen octahedra are rotating alternatively clockwise and anticlockwise. In order to ensure independent measurements, the columns of the same type are grouped in pairs. By assuming a fully periodic structure, the precision is measured in terms of the standard deviation on the determined value of the lattice parameter. For detecting significant differences between the techniques, 95% confidence intervals are calculated by using the following expression:

$$\sqrt{\frac{(n-1)s^2}{\chi^2_{n-1,0.025}}} \leq \sigma \leq \sqrt{\frac{(n-1)s^2}{\chi^2_{n-1,0.975}}} \tag{2}$$

with s^2 the sample variance and $\chi^2_{n-1,\alpha}$ the α quantile of the χ^2 distribution with $n-1$ degrees of freedom.

The results, summarized in Table 3, indicate that for all techniques a precision in the picometer range is obtained. In Section 5, it will be shown that when the precision in the images is only limited by Poisson noise, a much better precision can be obtained. Therefore, these values are most likely limited by image distortions such as scan distortions, sample drift or other mechanical and acoustical fluctuations. For the light oxygen columns, the precision is comparable for the different techniques. Here, small differences are most likely caused by image distortions, which differ per imaging technique. Contrary to the oxygen columns, the 95% confidence intervals show that the precision for the heavy A- and B-site columns in NCSI is significantly better as compared to the other techniques. This difference can be explained by the absence of a scanning process and therefore scan distortions.

Another remarkable results is observed in the precision of the heavy columns in the under focussed ISTEM image, which is worse as compared to the other techniques. These findings are in contradiction with van den Bos et al. [51], where it has been shown that atomic column positions can be measured with a better precision from ISTEM images as compared to HAADF STEM images. This contradiction can be explained by the used aperture setting in combination with the thickness of the investigated specimen, for which no defocus value has been found which results in a single image from which the positions of all different column types can be measured. As in the recorded under focussed ISTEM image still some contrast of the oxygen columns that are not modelled is remaining in the background, this most likely affects the precision with which the heavy A- and B-site column positions are measured.

In conclusion, these results indicate that without the use of post-processing techniques, NCSI provides the most precise measurements of the atomic column positions. One should, however, remark that precision is only important when results are accurate. The results in Section 4.1 indicate that the contrast

Technique	Precision A-site (pm)	Precision B-site (pm)	Precision O columns (pm)	Incoming dose ($e^-/Å^2$)
HAADF STEM	9.56 (*7.75 – 12.47*)	9.90 (*8.03 – 12.92*)	Not possible	7×10^4
LAADF STEM	12.15 (*9.85 – 15.84*)	12.65 (*10.26 – 16.50*)	Not possible	3.5×10^4
ABF STEM	9.85 (*7.99 – 12.85*)	10.88 (*8.82 – 14.19*)	14.21 (*12.10 – 17.21*)	7×10^4
iDPC STEM	12.83 (*10.41 – 16.74*)	10.87 (*8.82 – 14.18*)	18.88 (*16.08 – 22.86*)	3.5×10^4
NCSI	5.07 (*4.11 – 6.61*)	6.21 (*5.03 – 8.09*)	12.97 (*11.05 – 15.71*)	3.5×10^4
ISTEM in focus	Not possible	13.51 (*10.96 – 17.63*)	13.20 (*11.25 – 15.99*)	1.4×10^5
ISTEM underfocus	22.40 (*18.17 – 29.22*)	25.00 (*20.28 – 32.61*)	Not possible	1.4×10^5

Table 3: The precision with which the positions of an atomic column can be measured for the different experimental imaging techniques. The 95% confidence interval are shown in between the brackets. The incoming electron dose is presented in the last column. A much better precision is obtained when only Poisson noise is present (Section 5), indicating that the values presented in this Table are mainly limited by image distortions.

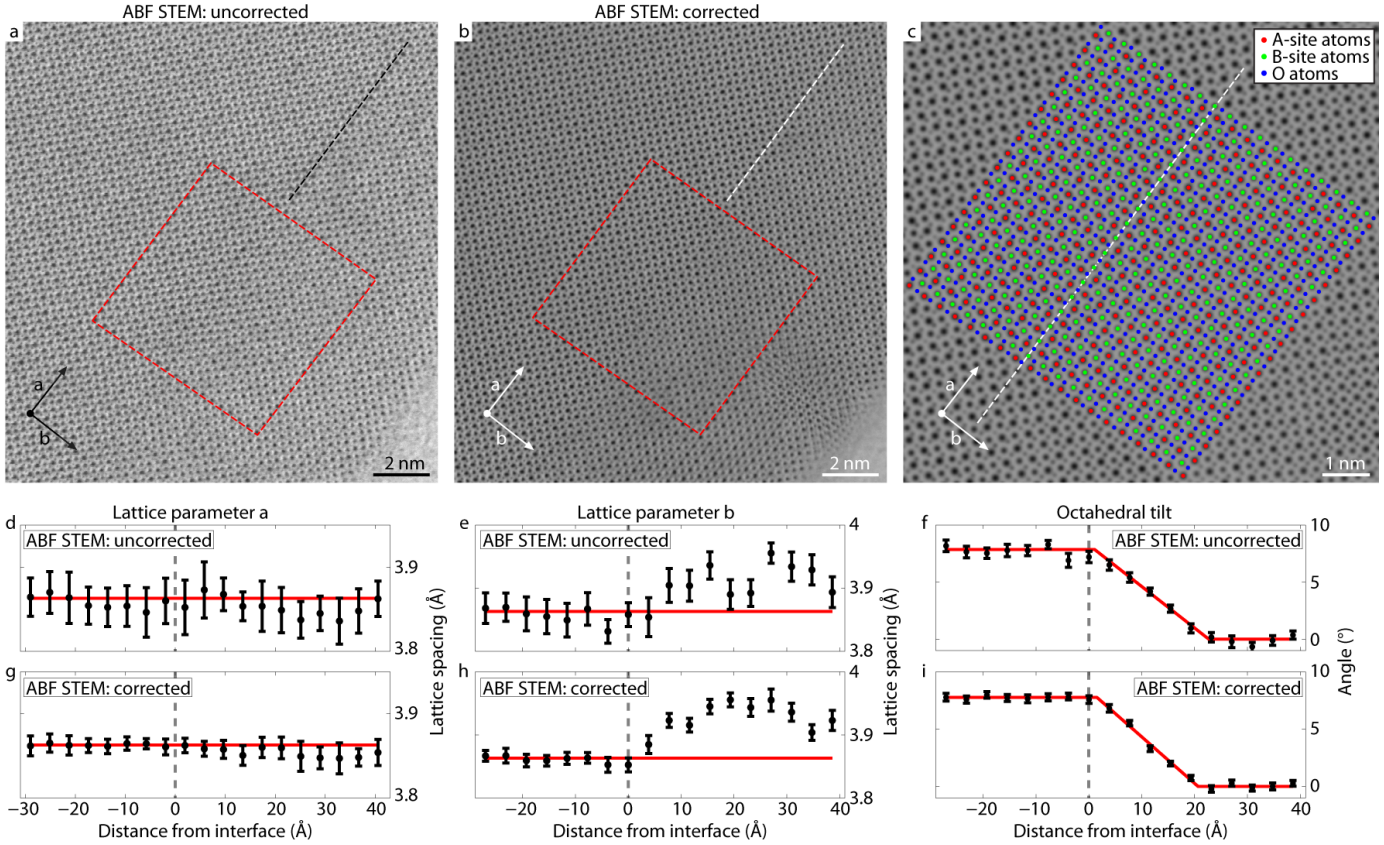

Figure 5: (a) The uncorrected and (b) corrected experimental ABF STEM image of the LSMO-NGO interface where the interface location is indicated by the black and white dotted lines, respectively. The uncorrected image is a single image from the time-series used to obtain the corrected image. (c) The fitted Gaussian model of the selected region in the corrected image (b) around the interface with the estimated column positions shown as an overlay. The white doted line marks the interface location. The mean lattice parameters (d,g) a and (e,h) b as a function of distance from the interface for the uncorrected and corrected images, respectively. The bulk reference lattice parameter of 3.863 Å is shown in red. (f,i) The mean tilt of the oxygen BO_6 octahedral as a function of distance from the interface for the uncorrected and corrected image, respectively. The red curves represent a ramp function that is fitted in order to characterise the octahedral tilt around the interface. The grey dashed lines mark the expected interface position.

in NCSI is highly sensitive to sample imperfections and microscope parameters, which can result in inaccurate measurements.

4.3. Distortion correction in ABF STEM

Mechanical and acoustical fluctuations in the surrounding environment of the microscope cause noise in the acquired images [58, 59]. Next to these environmental disturbances, sample drift and scan distortions are in STEM imaging important sources of image distortions. In TEM images this effect is less pronounced since the acquisition of a single shot image is usually much shorter than a STEM scan. As will be shown in Section 5, if only Poisson noise is present in the experimental images, a much better precision can be achieved. Therefore, a longer exposure time or a higher incident electron dose will not improve the results as image distortion will still limit the precision. In order to correct for image distortions, post-processing techniques which reduce the effect of these environmental disturbances are nowadays available [54, 60, 61, 62, 63]. Here, we test the effect of sample drift and scan distortions on an ABF

STEM image in order to demonstrate how a post-processing technique can improve results.

For applying the sample drift and scan distortion correction, 20 ABF STEM images are consecutively recorded. For each image of the time-series, the incoming dose has been set to 3.5×10^4 electrons per Å^2. The influence of sample drift during the acquisition of these experimental images can be post-compensated by finding the affine transformation $\mathbf{T}$, which minimizes the squared difference between two consecutive images. This affine transformation includes horizontal shear (α), vertical scaling (β), x shift (x_0) and y shift (y_0) between consecutive images:

$$\mathbf{T}\left(\begin{bmatrix} x \\ y \end{bmatrix}\right) = \begin{bmatrix} 1 & \alpha \\ 0 & \beta \end{bmatrix} \begin{bmatrix} x \\ y \end{bmatrix} + \begin{bmatrix} x_0 \\ y_0 \end{bmatrix} \tag{3}$$

The images are drift compensated by applying their corresponding affine transformations. Then an average image is calculated from the drift compensated images which is used to correct the scan distortions in each original image. The scan distortion compensation procedure for each image starts by applying its corresponding inverse affine transformation to the average image and finding a shift which minimizes the squared difference for each row between the average image and the processed image. Then scan distortions in each image are corrected by applying their corresponding shift row by row. Drift and scan distortion compensation procedures are performed iteratively until a stable average image is obtained.

In Fig. 5, the uncorrected ABF STEM image, which is a single image from the time-series, and the corrected image are shown together with the results of an analysis based on the lattice parameter and octahedral tilt across the interface. In section 4.1 and 4.2 the details for extracting these parameters are described. When comparing the profiles of the lattice parameters and octahedral tilt measured from the corrected image with the results from the uncorrected image, it can be noticed that the trend of the profiles is identical. As shown in Table 4, the region in LSMO that is affected by octahedral coupling is reduced to 5.0 unit cells, which matches better to the value found by Liao et al. [17]. The octahedral tilt in the NGO bulk part is not modified by the correction, indicating that the correction procedure does not change the accuracy of the results.

Since the measured octahedral tilt in the NGO bulk region remains slightly different as compared to the reference bulk value of 9° - 10° [55], it indicates that sample drift and scan distortion correction do not correct for this offset. Similar as in section 4.1.2, the measured tilt angle of the B-site atoms in the NGO bulk part is used to confirm that remaining image distortions are not causing such offsets (see Table 4). The profiles in Figs 5(f) and 5(i) show that the measured octahedral tilt in the NGO bulk part remains constant, which makes it most likely that all the measured oxygen column positions are shifted by the same amount. It was already mentioned in section 4.1.2 that small misalignments of the sample in the microscope can shift the peak intensity away from the centre of an atomic column [51, 56]. As this shift is constant for columns of the same type, it can explain the obtained shift in the measured oxygen column positions. More importantly, this indicates that ABF imaging is still suitable to characterize the changes in octahedral tilt along the interface on a relative basis, which is also confirmed by the match of the size of the affected region by octahedral coupling with literature.

Technique	Octahedral coupling	Bulk octahedral tilt	Bulk B-site tilt
Uncorrected	5.6 ± 1.0 UC	7.8° ± 0.3°	0.1° ± 0.2°
Corrected	5.0 ± 0.5 UC	7.8° ± 0.2°	0.01° ± 0.07°

Table 4: Different structure parameters of the LSMO-NGO sample extracted from the uncorrected and corrected ABF STEM image. The second column shows the region around the interface that is affected by octahedral coupling. The third column highlights the octahedral tilt of the oxygen columns in the NGO bulk material. The fourth column demonstrates that distortions do most likely not affect the extracted values as no tilt is present in the B-site columns.

As the column positions can be estimated with high accuracy, the precision of these measured column positions is determined. The major advantage of sample drift and scan distortion correction can be seen by the smaller error bars in the profiles shown in Fig. 5, indicating that it improves the precision of the measured column positions. Similar as in section 4.2, the precision is measured in terms of the standard deviation on the measured lattice parameter when grouping neighbouring columns of the same type together. Table 5 shows that the precision improves by more than a factor two as compared to an uncorrected image and that this improvement is significant because the 95% confidence intervals are not overlapping. Furthermore, when comparing the values to the results of NCSI from Table 3 a comparable precision is found, indicating that the precision in STEM imaging is mainly limited by sample drift and scan distortions, contrary to NCSI.

5. Ultimate precision

As technology is continuously improving, mechanical and electrical instabilities of transmission electron microscopes are playing a less and less dominant role for determining image precision. Therefore, image distortions that are nowadays present in images are likely to become negligible in a medium-term future. In this ultimate case, the precision limit in electron microscopy will only be determined by Poisson statistics. In order to investigate the differences between the techniques for this future scenario, the precision with which atomic columns can be measured is determined from image simulations containing only Poisson noise. Similar simulation parameters as described in Appendix A are used, where only the structure is replaced

Column	Uncorrected Precision (pm)	Corrected Precision (pm)
A-site	9.74 (*7.90 – 12.71*)	4.17 (*3.38 – 5.44*)
B-site	11.35 (*9.20 – 14.80*)	3.00 (*2.43 – 3.91*)
O	14.36 (*12.23 – 17.40*)	5.55 (*4.72 – 6.72*)

Table 5: The precision with which the positions of an atomic column can be measured for an uncorrected and corrected ABF STEM image. The 95% confidence interval are shown in between the brackets.

Technique	Precision (pm) A-site	Precision (pm) B-site	Precision (pm) O columns	Incoming dose (e^-/Å^2)
HAADF STEM	1.32 (*1.16 – 1.53*)	1.82 (*1.60 – 2.12*)	Not possible	3.5×10^4
LAADF STEM	1.15 (*1.01 – 1.34*)	1.62 (*1.42 – 1.89*)	Not possible	3.5×10^4
ABF STEM	1.93 (*1.70 – 2.25*)	3.48 (*3.05 – 4.04*)	4.82 (*4.23 – 5.60*)	3.5×10^4
iDPC STEM	2.30 (*2.02 – 2.67*)	1.68 (*1.48 – 1.96*)	0.97 (*0.85 – 1.13*)	3.5×10^4
NCSI	1.09 (*0.96 – 1.27*)	0.68 (*0.59 – 0.79*)	0.10 (*0.09 – 0.12*)	3.5×10^4
ISTEM in focus	0.86 (*0.75 – 1.00*)	0.48 (*0.42 – 0.56*)	0.20 (*0.18 – 0.23*)	3.5×10^4
ISTEM under focus	0.44 (*0.38 – 0.51*)	0.42 (*0.37 – 0.51*)	0.38 (*0.34 – 0.45*)	3.5×10^4

Table 6: The precision with which the positions of an atomic column can be measured from 100 noise realisations of simulated images of NGO by the different imaging techniques. The 95% confidence interval are shown in between the brackets. The incoming electron dose is presented in the last column.

by 4×4 unit cells of NGO on a supercell mesh of 1024×1024 pixels.

As demonstrated in the previous sections, all considered imaging techniques can accurately visualize light and heavy elements at the atomic scale. To investigate the precision with which atomic column positions can ultimately be measured, 100 different noise realisations for each imaging techniques have been evaluated. Here, only image, or shot, noise is modelled by using random Poisson distributed image pixel values. An incoming electron dose of 3.5×10^4 e$^-$/Å^2 has been used. For the iDPC technique, images recorded on the four quadrant detector have been modelled as Poisson distributed image pixel values detectors before processing the data to generate the final image. Similar as before, the precision is measured in terms of the standard deviation on the measured lattice parameter. Here, the two most central neighbouring columns of the same type are grouped together to calculate the lattice parameter. As the oxygen column positions are affected by octahedral tilt, the oxygen columns are paired with the second neighbouring unit cell (similar as in section 4.2).

The results in Table 6 indicate that several image distortions should still be present in all experimental images since the precision is much better as compared to the experimental values (see Table 3). In Section 4.3, it has been shown that sample drift and scan distortions are one of the main factors that affect the precision of the measured column positions in STEM imaging. However, the precision in case of the corrected image is still worse as compared to the precision measured in this section, indicating that, despite the large improvement, sample drift and scan distortion correction do not compensate for all present image distortions. Furthermore, other factors than sample drift and scan distortions may also affect the STEM images. Here, one could think of small misalignments of the microscope, crystal imperfections or other mechanical and acoustical fluctuations in the microscope components. For ISTEM, distortions seem to affect the experimental images even more, as the atomic column positions of all different types could not be estimated while in the simulations containing only shot noise this is possible. Since ISTEM is more robust towards probe instabilities and scan noise errors, it is expected that sample drift, crystal imperfections, small misalignments and mechanical and acoustical fluctuations in the microscope are the main causes for these distortions.

Table 6 shows that NCSI and ISTEM images give the best precision for measuring the atomic column positions. The 95% confidence intervals indicate that in most cases this improvement is significant as compared to HAADF, LAADF, ABF and iDPC STEM imaging. A possible explanation can be found in the recording mechanism, which is in NCSI and ISTEM imaging a CCD camera in the imaging plane recording the electrons that are scattered to relatively low angles. In the STEM based techniques, the detector records electrons scattered to a specific annular range, which is usually a higher annular regime as compared to NCSI and ISTEM. As the scattering to higher angles is less likely, NCSI and ISTEM imaging will record a higher number of scattered electrons as compared to these STEM based techniques in the same amount of time for the same incoming electron dose. Therefore, the Poisson statistics are better in the NCSI and ISTEM images resulting in more precise estimates.

It should, however, be noted that next to good Poisson statistics, also the contrast (peak-to-valley ratio) of the atomic columns plays a crucial factor in determining the precision. A first indication is given by a closer look at Table 6, which reveals that for almost every technique the precision with which atomic column positions can be measured is dependent on the atomic column type. Furthermore, the precision in ABF STEM imaging is worse as compared to ADF STEM imaging, while the number of recorded scattered electrons in ABF STEM imaging is higher as compared to ADF STEM imaging. These observation can only be explained by the image contrast, which differs per imaging technique as is known from the image simulations in Fig. 2 and the theory of image formation.

On average, under focussed ISTEM imaging gives the best precision for the different column types, indicating that this technique is most optimal to use. If one would purely focus on the oxygen column positions, then the results suggest that NCSI is the best option. In this future counting noise limited scenario, the results are only sensitive to microscope parameters and small improvements may be found by further optimising the microscope settings. As this improvements are expected to be small, this will not change the conclusions. As a final remark, it should be noted that these results are sample dependent and only hold for column positions measurements and cannot be extrapolated to other applications, such as for example atom counting.

6. Conclusions

In this work, a quantitative comparison has been made between LAADF STEM, ABF STEM, iDPC STEM, negative Cs TEM imaging and ISTEM, representing all the TEM techniques currently available and capable of visualizing light elements at the atomic scale. An interface of NGO and LSMO has been visualized by all these different techniques, where image simulations have been used to ensure optimal experimental conditions. Apart from the ADF STEM techniques, image simulations are essential for identifying the different column types as the image contrast depends on aberrations and is not always straightforward to interpret. This is especially the case for NCSI and ISTEM, as these techniques strongly depend on lens aberrations. For example, a different defocus could lead to contrast reversals. On the acquired experimental images, statistical parameter estimation theory has been used to enable a quantitative comparison between measured column positions.

It appears that the NCSI technique is less robust in terms of accuracy for the extraction of the atomic column positions as compared to the other techniques, especially at the interface location. This difference can be explained by the image contrast formation, which is for NCSI mostly dependent on the atomic column type, surface effects (local thickness and orientation variations) and microscope parameters (focus, astigmatism and comma). For the heavy A-site column positions, also inaccuracies have been observed when using the ISTEM images. This is explained by the recorded images, since it was not possible to acquire an image where all different atomic column types could provide interpretable contrast in a single frame. For light column position measurements ISTEM imaging provides, however, reliable results, since the octahedral tilt of the oxygen columns across the interface is determined accurately for ABF STEM, iDPC STEM, NCSI and ISTEM. As the results indicate that the atomic column positions of all types are measured accurately in the NGO bulk region, the precision with which atomic column positions can be measured is investigated.

All considered techniques provide somehow similar precisions, with the exception of NCSI imaging which is significantly better. This is most likely caused by the absence of a scanning process in this technique and a lower acquisition time as compared to STEM-based techniques, as sample drift and scan distortion correction from a time-series of ABF STEM images results in similar values as compared to NCSI. As technology is rapidly evolving, image distortions that are nowadays present in microscopy images are likely to become negligible in a medium-term future. Therefore, the ultimate precision for all studied techniques is determined by measuring column positions on simulated images of NGO containing only Poisson noise. As the obtained precisions are much smaller in comparison to both the uncorrected and corrected experimental values, the results suggest that distortions are indeed limiting the precision nowadays. It is, therefore, important to realize that imprecision in the STEM related techniques seems to not only be limited by sample drift and scanning distortions due to instrumental instabilities. In this future counting noise limited scenario, NCSI and ISTEM imaging will provide more precise values as compared to the other techniques, which can be understood from both the recording mechanism and the image contrast.

Despite their differences, all these techniques are providing correct and therefore reliable results. Especially with the presence of post-processing techniques, the precision with which atomic columns can be measured becomes comparable for all considered techniques. In order to improve the precision and to minimize experimental misconclusions, one has to keep in mind that several STEM based techniques can be combined in parallel as detectors are recording in different spatial regimes.

7. Acknowledgements

The authors acknowledge financial support from the Research Foundation Flanders (FWO, Belgium) through project fundings (G.0044.13N, G.0374.13N, G.0368.15N, G.0369.15N), and by a Ph.D. grant to K.H.W.v.d.B. The Qu-Ant-EM microscope used for this study was partly funded by the Hercules fund from the Flemish Government. A.B. and N.G. acknowledge the EUROTAPES project (FP7-NMP.2011.2.2-1 Grant no.280432) which partly funded this study. N.G., A.B. and J.V. acknowledge funding from the European Research Council under the 7th Framework Program (FP7), ERC Starting Grant 278510 VORTEX. The research leading to these results has received funding from the Deutsche Forschungsgemeinschaft under Contract No. RO 2057/4-2 and the European Union Seventh Framework Programme under Grant Agreement 312483 - ESTEEM2. We thank Prof. G. Koster from the University of Twente for kindly providing us with the LSMO-NGO test sample.

Appendix A. Simulation parameters

For finding the optimal settings in the microscope and identifying the different atomic column types, image simulations have been performed. A DFT simulation of an LSMO-NGO interface has been used to determine the 3D positions of all the atoms [17]. The simulation parameters for the different techniques are summarized in Table A.1.

Appendix B. Octahedral tilt measurements

In Section 4.1.2 it has been shown that the error on the measured octahedral tilt values differs per technique. In order to retrieve the origin of this difference, Fig. B.1 shows the measured octahedral tilt as a function of distance from the interface obtained in 3 different manners. First, the angle of the 2 oxygen columns parallel to a-direction with respect to this a-direction is measured. Next, the angle of the 2 oxygen columns perpendicular to this a-direction is determined with respect to the b-direction. Finally, the measured values of both directions are combined, as is described in Section 4.1.2. For iDPC STEM and ISTEM, both the parallel and perpendicular profiles are overlapping, while for ABF STEM small differences are observed. Since the parallel and perpendicular profiles in the corrected ABF STEM images are overlapping, the difference between the parallel and perpendicular profiles in the uncorrected

General	Acceleration voltage	300 kV
	Cs condenser	0.50 μm
	Source extent	0.034 nm
STEM techniques	Probe semi-angle	19.8 mrad
	Defocus	-10 nm
	Scan points	600×380
	Pixel size	0.1022 Å
NCSI	Cs imaging	-13 μm
	Objective aperture	27.9 mrad
ISTEM	Probe semi-angle	8 mrad
	Cs imaging	2 μm
	Objective aperture	60 mrad
Structure	Zone axis	[100]
	Supercell size	38.6×61.7 Å^2
	Supercell mesh	1150×1800
	Specimen thickness	16.14 nm
	DW-factor Na	0.7 Å^2
	DW-factor Ga	0.5 Å^2
	DW-factor O	0.74 Å^2
	DW-factor La	0.6 Å^2
	DW-factor Sr	0.62 Å^2
	DW-factor Mn	0.44 Å^2

Table A.1: Parameters for the multislice simulations of the different techniques for the LSMO-NGO interface using the STEMsim software.

ABF STEM is most likely caused by sample drift and scanning distortions. For NCSI, there is a large difference between the parallel and perpendicular profiles, indicating that the measured oxygen column positions are most likely affected by image distortions. This difference can be explained by the image formation process, which is for TEM imaging more sensitive to surface effects of the sample and aberrations of the objective lens [31, 32]. Furthermore, the column positions are highly sensitive to misalignments of the sample [51]. As a result, it is expected that the NCSI images are less robust in terms of accuracy as compared to the images acquired by the other techniques.

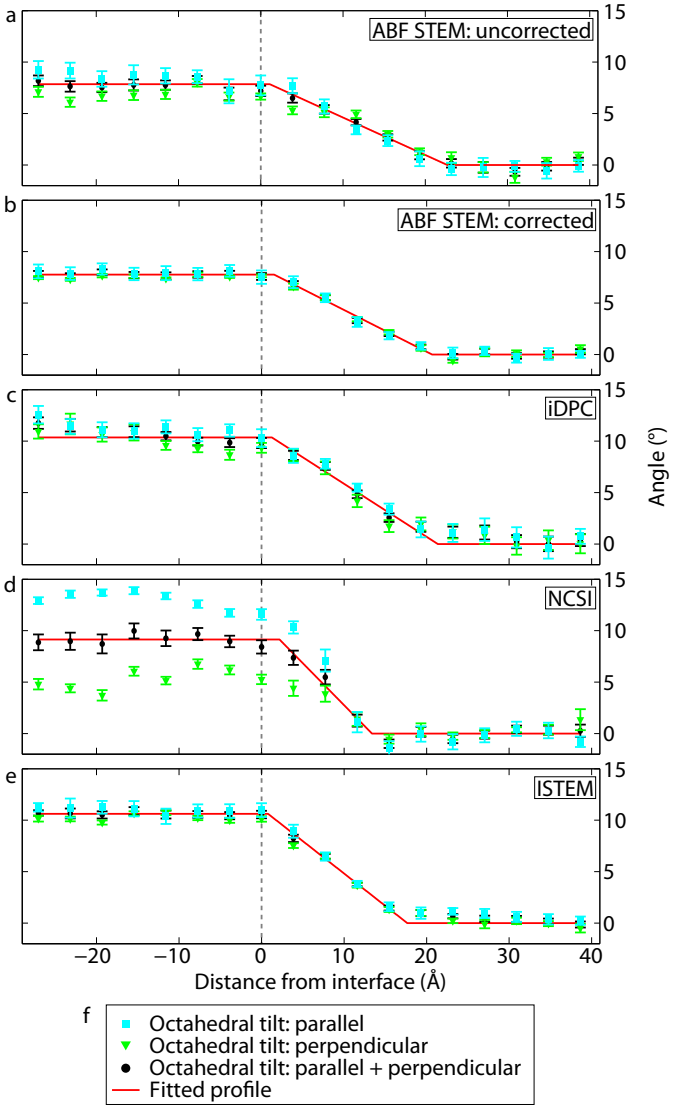

Figure B.1: (a-e) The mean octahedral tilt of the oxygen BO6 octahedron as a function of distance from the interface for the different imaging techniques. (f) The octahedral tilt is measured from the 2 oxygen columns neighbouring the B-site column in parallel and perpendicular direction with respect to the measured a-direction. The red curve represents the ramp function that has been fitted in Section 4.1.2 to the octahedral tilt measured by combining both the parallel and perpendicular measurements. The grey dashed lines mark the expected interface position.

References

[1] M. Lorenz, M. S. Ramachandra Rao, T. Venkatesan, E. Fortunato, P. Barquinha, R. Branquinho, D. Salgueiro, R. Martins, E. Carlos, A. Liu, F. K. Shan, M. Grundmann, H. Boschker, J. Mukherjee, M. Priyadarshini, N. DasGupta, D. J. Rogers, F. H. Teherani, E. V. Sandana, P. Bove, K. Rietwyk, A. Zaban, A. Veziridis, A. Weidenkaff, M. Muralidhar, M. Murakami, S. Abel, J. Fompeyrine, J. Zuniga-Perez, R. Ramesh, N. A. Spaldin, S. Ostanin, V. Borisov, I. Mertig, V. Lazenka, G. Srinivasan, W. Prellier, M. Uchida, M. Kawasaki, R. Pentcheva, P. Gegenwart, F. Miletto Granozio, J. Fontcuberta, N. Pryds, The 2016 oxide electronic materials and oxide interfaces roadmap, Journal of Physics D: Applied Physics 49 (43) (2016) 433001.

[2] J. Mannhart, D. G. Schlom, Oxide interfacesan opportunity for electronics, Science 327 (5973) (2010) 1607–1611.

[3] H. Y. Hwang, Y. Iwasa, M. Kawasaki, B. Keimer, N. Nagaosa, Y. Tokura, Emergent phenomena at oxide interfaces, Nature materials 11 (2) (2012) 103–113.

[4] A. Ohtomo, H. Y. Hwang, A high-mobility electron gas at the laalo3/srtio3 heterointerface, Nature 427 (6973) (2004) 423–426.

[5] H. Zhang, N. Gauquelin, G. A. Botton, J. Y. T. Wei, Attenuation of superconductivity in manganite/cuprate heterostructures by epitaxially-induced cuo intergrowths, Applied Physics Letters 103 (5) (2013) 052606.

[6] J. Chakhalian, J. W. Freeland, G. Srajer, J. Strempfer, G. Khaliullin, J. C. Cezar, T. Charlton, R. Dalgliesh, C. Bernhard, G. Cristiani, H.-U. Habermeier, B. Keimer, Magnetism at the interface between ferromagnetic and superconducting oxides, Nature Physics 2 (4) (2006) 244–248.

[7] T. Y. Chien, L. F. Kourkoutis, J. Chakhalian, B. Gray, M. Kareev, N. P. Guisinger, D. A. Muller, J. W. Freeland, Visualizing short-range charge transfer at the interfaces between ferromagnetic and superconducting oxides, Nature communications 4 (2013) 2336.

[8] V. Garcia, M. Bibes, Ferroelectric tunnel junctions for information storage and processing, Nature communications 5 (2014) 4289.

[9] I. D. Brown, Chemical and steric constraints in inorganic solids, Acta

Crystallographica Section B: Structural Science 48 (5) (1992) 553–572.
[10] A. M. Glazer, Simple ways of determining perovskite structures, Acta Crystallographica Section A: Crystal Physics, Diffraction, Theoretical and General Crystallography 31 (6) (1975) 756–762.
[11] P. M. Woodward, Octahedral tilting in perovskites. i. geometrical considerations, Acta Crystallographica Section B: Structural Science 53 (1) (1997) 32–43.
[12] P. M. Woodward, Octahedral tilting in perovskites. ii. structure stabilizing forces, Acta Crystallographica Section B: Structural Science 53 (1) (1997) 44–66.
[13] Y.-M. Kim, A. Kumar, A. Hatt, A. N. Morozovska, A. Tselev, M. D. Biegalski, I. Ivanov, E. A. Eliseev, S. J. Pennycook, J. M. Rondinelli, S. V. Kalinin, A. Y. Borisevich, Interplay of octahedral tilts and polar order in bifeo3 films, Advanced Materials 25 (17) (2013) 2497–2504.
[14] J. M. Rondinelli, S. J. May, J. W. Freeland, Control of octahedral connectivity in perovskite oxide heterostructures: An emerging route to multifunctional materials discovery, MRS bulletin 37 (3) (2012) 261–270.
[15] D. Kan, R. Aso, R. Sato, M. Haruta, H. Kurata, Y. Shimakawa, Tuning magnetic anisotropy by interfacially engineering the oxygen coordination environment in a transition metal oxide, Nature materials 15 (4) (2016) 432–437.
[16] Z. Liao, R. J. Green, N. Gauquelin, S. Macke, L. Li, J. Gonnissen, R. Sutarto, E. P. Houwman, Z. Zhong, S. Van Aert, J. Verbeeck, M. H. Sawatzky, G. Koster, G. Rijnders, Long-range domain structure and symmetry engineering by interfacial oxygen octahedral coupling at heterostructure interface, Advanced Functional Materials 26 (36) (2016) 6627–6634.
[17] Z. Liao, M. Huijben, Z. Zhong, N. Gauquelin, S. Macke, R. J. Green, S. Van Aert, J. Verbeeck, G. Van Tendeloo, K. Held, G. A. Sawatzky, G. Koster, G. Rijnders, Controlled lateral anisotropy in correlated manganite heterostructures by interface-engineered oxygen octahedral coupling, Nature materials 15 (4) (2016) 425–431.
[18] S. Macke, A. Radi, J. E. Hamann-Borrero, A. Verna, M. Bluschke, S. Brück, E. Goering, R. Sutarto, F. He, G. Cristiani, M. Wu, E. Benckiser, H.-U. Habermeier, G. Logvenow, N. Gauquelin, G. A. Botton, A. P. Kajdos, S. Stemmer, G. A. Sawatzky, M. W. Haverkort, B. Keimer, V. Hinkov, Element specific monolayer depth profiling, Advanced Materials 26 (38) (2014) 6554–6559.
[19] H. H. Rose, Optics of high-performance electron microscopes, Science and Technology of Advanced Materials 9 (1) (2008) 014107.
[20] H. H. Rose, Historical aspects of aberration correction, Journal of electron microscopy (2009) dfp012.
[21] O. L. Krivanek, N. Dellby, M. F. Murfitt, Aberration correction in electron microscopy, in: J. Orloff (Ed.), Handbook of Charged Particle Optics, CRC Press, 2009, pp. 601–641.
[22] C. Kisielowski, C. J. D. Hetherington, Y. C. Wang, R. Kilaas, M. A. O'Keefe, A. Thust, Imaging columns of light elements carbon, nitrogen and oxygen with sub ångstom resolution, Ultramicroscopy 89 (2001) 243–263.
[23] K. W. Urban, Studying atomic structures by aberration-corrected transmission electron microscopy, Science 321 (5888) (2008) 506–510.
[24] R. Erni, M. D. Rossell, C. Kisielowski, U. Dahmen, Atomic-resolution imaging with a sub-50-pm electron probe, Physical Review Letters 102 (2009) 096101.
[25] A. Lotnyk, D. Poppitz, J. W. Gerlach, B. Rauschenbach, Direct imaging of light elements by annular dark-field aberration-corrected scanning transmission electron microscopy, Applied Physics Letters 104 (7) (2014) 071908.
[26] S. D. Findlay, N. Shibata, H. Sawada, E. Okunishi, Y. Kondo, Y. Ikuhara, Dynamics of annular bright field imaging in scanning transmission electron microscopy, Ultramicroscopy 110 (7) (2010) 903–923.
[27] S. D. Findlay, Y. Kohno, L. A. Cardamone, Y. Ikuhara, N. Shibata, Enhanced light element imaging in atomic resolution scanning transmission electron microscopy, Ultramicroscopy 136 (2014) 31–41.
[28] I. Lazić, E. G. T. Bosch, S. Lazar, Phase contrast stem for thin samples: Integrated differential phase contrast, Ultramicroscopy 160 (2016) 265–280.
[29] H. Rose, Phase contrast in scanning transmission electron microscopy, Optik 39 (4) (1974) 416–436.
[30] N. Shibata, S. D. Findlay, Y. Kohno, H. Sawada, Y. Kondo, Y. Ikuhara, Differential phase-contrast microscopy at atomic resolution, Nature Physics 8 (8) (2012) 611–615.
[31] C.-L. Jia, M. Lentzen, K. Urban, High-resolution transmission electron microscopy using negative spherical aberration, Microscopy and Microanalysis 10 (02) (2004) 174–184.
[32] K. W. Urban, C.-L. Jia, L. Houben, M. Lentzen, S.-B. Mi, K. Tillmann, Negative spherical aberration ultrahigh-resolution imaging in corrected transmission electron microscopy, Philosophical Transactions of the Royal Society of London A: Mathematical, Physical and Engineering Sciences 367 (1903) (2009) 3735–3753.
[33] A. Rosenauer, F. F. Krause, K. Mller, M. Schowalter, T. Mehrtens, Conventional Transmission Electron Microscopy Imaging beyond the Diffraction and Information Limits, Physical Review Letters 113 (096101).
[34] D. A. Muller, Why changes in bond lengths and cohesion lead to core-level shifts in metals, and consequences for the spatial difference method, Ultramicroscopy 78 (1) (1999) 163–174.
[35] C. Kisielowski, E. Principe, B. Freitag, D. Hubert, Benefits of microscopy with super resolution, Physica B: Condensed Matter 308 (2001) 1090–1096.
[36] A. J. den Dekker, S. Van Aert, A. van den Bos, D. Van Dyck, Maximum likelihood estimation of structure parameters from high resolution electron microscopy images. Part I: A theoretical framework, Ultramicroscopy 104 (2005) 83–106.
[37] S. Van Aert, A. J. den Dekker, A. van den Bos, D. Van Dyck, J. H. Chen, Maximum likelihood estimation of structure parameters from high resolution electron microscopy images: Part II: A practical example, Ultramicroscopy 104 (2005) 107–125.
[38] S. Van Aert, J. Verbeeck, R. Erni, S. Bals, M. Luysberg, D. Van Dyck, G. Van Tendeloo, Quantitative atomic resolution mapping using high-angle annular dark field scanning transmission electron microscopy, Ultramicroscopy 109 (2009) 1236–1244.
[39] A. De Backer, K. H. W. van den Bos, W. Van den Broek, J. Sijbers, S. Van Aert, Statstem: An efficient approach for accurate and precise model-based quantification of atomic resolution electron microscopy images, Ultramicroscopy 171 (2016) 104–116.
[40] J. Gonnissen, A. De Backer, A. J. den Dekker, G. T. Martinez, A. Rosenauer, J. Sijbers, S. Van Aert, Optimal experimental design for the detection of light atoms from high-resolution scanning transmission electron microscopy images, Applied Physics Letters 105 (063116).
[41] J. Gonnissen, A. De Backer, A. den Dekker, J. Sijbers, S. Van Aert, Detecting and locating light atoms from high-resolution stem images: The quest for a single optimal design, Ultramicroscopy 170 (2016) 128–138.
[42] H. Rose, Nonstandard imaging methods in electron microscopy, Ultramicroscopy 2 (1976) 251–267.
[43] K. Müller-Caspary, F. F. Krause, T. Grieb, S. Löffler, M. Schowalter, A. Béché, V. Galioit, D. Marquardt, J. Zweck, P. Schattschneider, J. Verbeeck, A. Rosenauer, Measurement of atomic electric fields and charge densities from average momentum transfers using scanning transmission electron microscopy, Ultramicroscopy in Press.
[44] M. Lentzen, B. Jahnen, C. L. Jia, A. Thust, K. Tillmann, K. Urban, High-resolution imaging with an aberration-corrected transmission electron microscope, Ultramicroscopy 92 (3) (2002) 233–242.
[45] C. L. Jia, S. B. Mi, M. Faley, U. Poppe, J. Schubert, K. Urban, Oxygen octahedron reconstruction in the SrTiO3/LaAlO3 heterointerfaces investigated using aberration-corrected ultrahigh-resolution transmission electron microscopy, Physical Review B 79 (8) (2009) 081405.
[46] C. L. Jia, L. Houben, A. Thust, J. Barthel, On the benefit of the negative-spherical-aberration imaging technique for quantitative hrtem, Ultramicroscopy 110 (5) (2010) 500–505.
[47] A. Rosenauer, M. Schowalter, Stemsim - a new software tool for simulation of STEM HAADF Z-contrast imaging, in: A. Cullis, P. Midgley (Eds.), Microscopy of Semiconducting Materials 2007, Vol. 120 of Springer Proceedings in Physics, Springer Netherlands, 2008, pp. 170–172.
[48] A. Rosenauer, M. Schowalter, J. Titantah, D. Lamoen, An emission-potential multislice approximation to simulate thermal diffuse scattering in high-resolution transmission electron microscopy, Ultramicroscopy 108 (2008) 1504–1513.
[49] S. Bals, S. Van Aert, G. Van Tendeloo, D. Ávila-Brande, Statistical estimation of atomic positions from exit wave reconstruction with a precision in the picometer range, Physical Review Letters 96 (2006) 096106.
[50] A. De Backer, S. Van Aert, D. Van Dyck, High precision measurements

of atom column positions using model-based exit wave reconstruction, Ultramicroscopy 111 (2011) 1475–1482.
[51] K. H. W. van den Bos, F. F. Krause, A. Béché, J. Verbeeck, A. Rosenauer, S. Van Aert, Locating light and heavy atomic column positions with picometer precision using ISTEM, Ultramicroscopy 172 (2017) 75–81.
[52] K. Kimoto, T. Asaka, X. Yu, T. Nagai, Y. Matsui, K. Ishizuka, Local crystal structure analysis with several picometer precision using scanning transmission electron microscopy, Ultramicroscopy 110 (2010) 778–782.
[53] Y.-M. Kim, J. He, M. D. Biegalski, H. Ambaye, V. Lauter, H. M. Christen, S. T. Pantelides, S. J. Pennycook, S. V. Kalinin, A. Y. Borisevich, Probing oxygen vacancy concentration and homogeneity in solid-oxide fuell-cell cathode materials on the subunit-cell level, Nature Materials 11 (2012) 888–894.
[54] A. B. Yankovich, B. Berkels, W. Dahmen, P. Binev, S. I. Sanchez, S. A. Bradley, A. Li, I. Szlufarska, Voy, Picometre-precision analysis of scanning transmission electron microscopy images of platinum nanocatalysts, Nature Communications 5 (2014) 4155.
[55] W. Marti, P. Fischer, F. Altorfer, H. Scheel, M. Tadin, Crystal structures and phase transitions of orthorhombic and rhombohedral rgao3 (r= la, pr, nd) investigated by neutron powder diffraction, Journal of Physics: Condensed Matter 6 (1) (1994) 127.
[56] D. Zhou, K. Mller-Caspary, W. Sigle, F. F. Krause, A. Rosenauer, P. A. van Aken, Sample tilt effects on atom column position determination in abfstem imaging, Ultramicroscopy 160 (2016) 110–117.
[57] Y. Liu, Y. L. Zhu, Y. L. Tang, X. L. Maa, An effect of crystal tilt on the determination of ions displacements in perovskite oxides under BF/HAADF-STEM imaging mode, Journal of Materials Research (2016) 1–10.
[58] H. S. von Harrach, Instrumental factors in high-resolution feg stem, Ultramicroscopy 58 (1995) 1–5.
[59] D. A. Muller, E. J. Kirkland, M. G. Thomas, J. L. Grazul, L. Fitting, M. Weyland, Room design for high-performance electron microscopy, Ultramicroscopy 106 (2006) 1033–1040.
[60] L. Jones, P. D. Nellist, Identifying and Correcting Scan Noise and Drift in the Scanning Transmission Electron Microscope, Microscopy and Microanalysis 19 (2013) 1050–1060.
[61] X. Sang, J. M. LeBeau, Revolving scanning transmission electron microscopy: correcting sample drift distortion without prior knowledge, Ultramicroscopy 138 (2014) 28–35.
[62] L. Jones, H. Yang, T. J. Pennycook, S. J. Marshall, S. Van Aert, N. D. Browning, M. R. Castell, P. D. Nellist, Smart Align - a new tool for robust non-rigid registration of scanning microscope data, Advanced Structural and Chemical Imaging 1 (2015) 8.
[63] C. Ophus, J. Ciston, C. T. Nelson, Correcting nonlinear drift distortion of scanning probe and scanning transmission electron microscopies from image pairs with orthogonal scan directions, Ultramicroscopy 162 (2016) 1–9.